



Multi-scale modeling and simulation of IR radiative drying for coil coating processes

Beatriz S. Dias, Jorge E. P. Navalho & José C. F. Pereira

To cite this article: Beatriz S. Dias, Jorge E. P. Navalho & José C. F. Pereira (2022) Multi-scale modeling and simulation of IR radiative drying for coil coating processes, *Drying Technology*, 40:16, 3466-3482, DOI: [10.1080/07373937.2022.2055055](https://doi.org/10.1080/07373937.2022.2055055)

To link to this article: <https://doi.org/10.1080/07373937.2022.2055055>



© 2022 The Author(s). Published with license by Taylor and Francis Group, LLC



Published online: 12 Apr 2022.



Submit your article to this journal [↗](#)



Article views: 937



View related articles [↗](#)



View Crossmark data [↗](#)



Citing articles: 1 View citing articles [↗](#)

Multi-scale modeling and simulation of IR radiative drying for coil coating processes

Beatriz S. Dias, Jorge E. P. Navalho, and José C. F. Pereira

IDMEC, Instituto Superior Técnico, Universidade de Lisboa, Lisboa, Portugal

ABSTRACT

The present work reports the development of a multi-scale model to predict and control the drying behavior of a coated substrate under infrared (IR) radiant burners. The model accounts for simultaneous heat and mass transfer in a liquid film layer, characterized by a binary polymer-solvent solution. The multi-scale model developed works with two distinguished scales, a micro(coating film)- and a macro(oven)-scale, which are connected by an iterative two-way coupling procedure. Along iterations of the coupling procedure the solution converges until it fulfills the convergence parameter prescribed. The model is widely validated with reference results and inspecting convergence criterion. Parametric studies are performed to investigate the effect of radiative over convective heating and the influence of specific oven operating conditions. It follows that drying by means of radiative energy minimizes the energy consumption, lowers the drying time, and higher drying efficiencies are achieved than with conventional convective drying.

ARTICLE HISTORY

Received 1 December 2021
Revised 31 January 2022
Accepted 15 March 2022

KEYWORDS

Drying model; Multi-scale modeling; Radiative heating; Binary polymer-solvent solution; Coil coating

1. Introduction

Drying of polymer-solvent solutions plays an important role in several modern industrial applications, namely on the coil coating industrial process. The ability to foresee the drying behavior of coatings is of extreme importance to the coating industry. The optimization of industrial drying processes needs to ensure the maximum evaporation of solvent, or moisture content, in the shortest time possible with the minimal energy consumption, while maintaining the product quality [1].

Coil coatings, or in other words, pre-coated metal sheets, have drawn attention during the last decades to protect and increase the corrosion-resistance and durability of many materials widely used in automotive, building, furniture, and many other sectors [2, 3]. Some of the requirements of coatings are good adherence to the metal substrate, great resistance to the environment, and an agreeable flexibility that permits a 180° folding of the sheet without any crack [3].

The coil coating process involves the application of a thin layer of an organic coating material on a moving metal strip, and this layer is dried, generally, in an oven with forced air convection [4–6]. In the drying/curing process, which occurs inside a curing oven, organic solvents are vaporized from the applied liquid

coating film. The coil coating lines employ high-temperature ovens to achieve cure at the required speed. The energy needed to vaporize the solvents usually comes from the heat by convection [4].

Over the last years there has been a great interest concerning the potential for radiation curing, including for coil coatings. The attractive benefits include very rapid curing, reduced energy input, less environmental volatile organic compounds (VOCs) impact, reduced space usage, and better controllability [7]. Each paint needs its technology, and the infrared is appropriated for solvent coatings while radiation curable coatings using ultraviolet or electron beam exposure do not contain the solvents [8, 9]. However there are scarce experimental data on the effect of infrared radiation on drying rates. A few and exploratory infrared cure experimental studies have been reported for the infrared cure cycle of a powder coating [10] and for the near infrared radiation (NIR) heating performance and the influence of a coating's optical properties on curing [11].

Infrared radiation as an energy source for drying processes is drawing each day more attention, since heat is transferred efficiently, products are heated more uniformly, and the costs involved in processing are lower

CONTACT Jorge E. P. Navalho  jorge.navalho@tecnico.ulisboa.pt

© 2022 The Author(s). Published with license by Taylor and Francis Group, LLC

This is an Open Access article distributed under the terms of the Creative Commons Attribution-NonCommercial-NoDerivatives License (<http://creativecommons.org/licenses/by-nc-nd/4.0/>), which permits non-commercial re-use, distribution, and reproduction in any medium, provided the original work is properly cited, and is not altered, transformed, or built upon in any way.

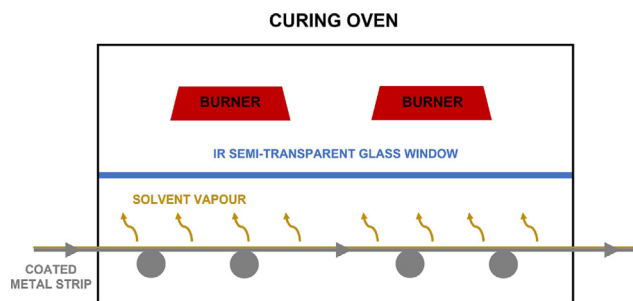


Figure 1. Proposed concept of curing oven for coil coating process.

than with conventional drying by hot air convection [12, 13]. Kowalski and Rajewska [14] showed that combining convective-microwave, convective-infrared, and convective-microwave-infrared drying processes results in high drying rates while conserving a good quality of the dried product. A recent study [15] was conducted to compare drying by hot-air flow and by infrared irradiation, while controlling drying conditions to achieve comparable drying rates. The temperature of the drying film was found to be lower in drying by hot-air and the temperature gradients were minimal in drying by infrared irradiation. Later, an investigation assisted the design and optimization of the drying with design space calculation [16]. Wen *et al.* [17] studied the effects of infrared radiation-hot air (IR-HA) drying on kinetic models and concluded that IR-HA drying increased the drying rates as well as the effective transport (diffusion) coefficients in comparison with hot-air drying alone. Additionally, lower drying times, higher energy savings, and a better final product quality are advantages of infrared drying over convective drying [18].

A novel procedure is proposed [7] to heat the metal strip by infrared (IR) radiation, performing the drying and curing process in an atmosphere mainly consisting of solvent vapors. The principal source of energy for drying/curing of the coating is supplied by IR radiant burners that provide high intensity IR-radiation. Compared to conventional convective ovens, heat fluxes are increased to the coated metal strip and the necessary curing temperatures at the surface of the strip can be reached faster. The novel procedure aims not only to increase the compactness and energetic efficiency of the system, but also leads to an increase on the production flexibility.

Figure 1 shows schematically the proposed curing oven with IR radiant burners. An IR semi-transparent glass window is needed to ensure the environments separation, which avoids the mixing of solvent vapor with combustion gases. The control and analysis of the drying behavior is of extreme importance to assure the safety requirements are met.

The drying behavior of polymer coatings involves two steps: transport of the solvent(s) toward the surface; and solvent(s) removal from the surface [5]. For polymer-solvent systems, the solvent diffuses through the coating owing to its concentration gradient. Several articles in the literature address different models for drying the polymeric solutions. Infrared (IR) radiant heating is used to supplement the heat source on a drying process with natural convection and/or forced convection [19]. Kumar and Tien [20] present a complete model of the interaction of radiative flux with convective transport in an absorbing, emitting, and scattering falling film. Lamaison *et al.* [21] and Navarri and Andrieu [22] described infrared drying of a painting and a PVA coating. Allanic *et al.* [23] studied the drying behavior of PVA aqueous solution placed into a Petri box, and present drying kinetics in convective and infrared radiation. Chen and Lin [24], Seyed-Yagoobi and Hussain [25], and Allanic *et al.* [26] took into consideration the absorption of IR radiant energy into the water, in order to perform a more accurate heat transfer analysis for the IR-assisted drying in the forced convection regime [19].

Cairncross *et al.* [27] modeled a multi-zone industrial dryer with convective and radiant heating, considering the transient 1D convection-diffusion equations of heat and mass transfer. The absorption of radiation through the coating was described by Lambert-Beer law. Islam *et al.* [28] presents the dynamic modeling of drying behavior of a PVAC coating (in toluene) on a polyester substrate in an infrared-convective oven. Allanic *et al.* [29] investigated the drying and curing of PU water based varnish by IR radiation. Some experiments of convective and IR-convective drying have been performed, along with the development of a model to determine the evolution of moisture content, diffusivity, and temperature of the product.

Most often, coil coating lines used in industry are forced-convection dryers, where hot air is blown across the film to evaporate the solvent. The present methodology aims to extend the knowledge about coil coating industrial lines using a source of energy for drying/curing of the coating supplied by IR radiant burners. The present methodology eliminates the need for forced convection and has direct solvent recovery because the solvent feeds and is burnt in the radiant porous burners. Consequently, the detrimental environmental effects from volatile organic compounds escaping into the atmosphere are minimized.

The main objectives of the present work are two-fold. The first is to develop and validate a multi-scale model comprising micro- and macro-scale models.

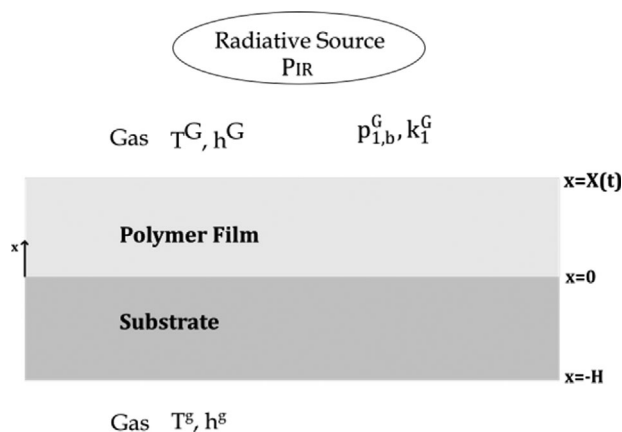


Figure 2. Schematic of 1D drying geometry.

The micro-scale model comprises the transient drying equations of a binary polymer-solvent coating, which involves simultaneous mass, energy, and momentum transport [30]. The macro-scale model comprises the oven mathematical models and associated transport phenomena to calculate fluid flow, heat transfer, and radiation over the moving coil in the oven. The second objective is to apply the developed multi-scale methodology to demonstrate some of the differences between conventional and radiation-curing systems in a coil coating virtual application and to conduct a parametric study to oven operating conditions of a virtual coating line. This work contributes to fill the gap in the literature concerning the lack of work applying fully predictive multi-scale models and radiative heat source for solvent evaporation (film drying), particularly, for coil coating industrial applications.

This paper is structured in four sections. The current section focuses in presenting the subject, as well as its relevance to the field of expertise. Section 2 presents the multi-scale modeling displaying the main mathematical equations, the numerical model adopted, and the proposed methodology for the iterative two-way coupling procedure. The results of the multi-scale model (Section 3) begin with the validation of the micro-scale model, following an application of the multi-scale methodology developed, as well as a comparison study between convection and radiation, and ends with the overall performance in the coil coating IR radiation process. Finally, this paper ends in Section 4 with summary conclusions.

2. Mathematical and numerical models

2.1. Micro-scale model: drying film model

The equations governing the drying of a binary polymer solution (wet coating) are the mass and energy

balance equations. In the current work, both balance equations are solved transiently and along the thickness of the polymer layer – 1D (one-dimensional) model, as represented in Figure 2.

2.1.1. Mass balance

The species continuity equation for the solvent is defined along the thickness, $0 < x < X(t)$, as given by Equation (1).

$$\frac{\partial \rho_1^p}{\partial t} = \frac{\partial}{\partial x} \left(D^p \frac{\partial \rho_1^p}{\partial x} \right) \quad (1)$$

In this equation, ρ_1^p is the mass density (concentration) of the solvent species in the polymer solution, t and x are the temporal and spatial coordinates, respectively, and D^p corresponds to the solvent-polymer mutual diffusion coefficient. The coating/substrate interface is impermeable, and consequently, there is no transport of solvent into the substrate layer. Therefore, at the coating/substrate interface ($x = 0$), Equation (2) holds.

$$\frac{\partial \rho_1^p}{\partial x} = 0 \quad (2)$$

At the coating/gas interface ($x = X(t)$), the application of a solvent species mass balance leads to Equation (3). In this equation, k_1^G , p_{1i}^G , and p_{1b}^G are the external mass transport coefficient, equilibrium solvent pressure at the coating/gas interface, and solvent pressure in the bulk gas, respectively.

$$-D^p \frac{\partial \rho_1^p}{\partial x} - \rho_1^p \frac{dX}{dt} = k_1^G (p_{1i}^G - p_{1b}^G) \quad (3)$$

Equation (3) takes into account the diffusion of species from the polymer layer, the temporal rate of shrinking of the polymer layer, and the external transport of solvent species across the surrounding boundary layer from the free polymer layer surface (coating/gas interface). The driving force for solvent evaporation and film drying is the solvent concentration difference between the bulk gas and surface values.

Equation (4) represents the time dependence of the film thickness, or in other words, the governing equation for the position of the interface. In this equation, \hat{V}_1^p is the partial specific volume of solvent in the solution. The initial coating thickness is known, $X(0) = L$, and the initial solvent concentration throughout the coating ($0 < x < X(t)$) is uniform, $\rho_1^p(0, x) = \rho_{1,0}^p$.

$$\frac{dX}{dt} = -k_1^G \hat{V}_1^p (p_{1i}^G - p_{1b}^G) \quad (4)$$

The concentration and temperature dependence of the diffusion coefficients is taken into account in

accordance to Vrentas-Duda free volume theory [31]. The equation for the solvent self-diffusion coefficient is given by Equation (5), where the hole free volume is provided by Equation (6).

$$D_1 = D_0 \exp\left(\frac{-E_a}{RT}\right) \exp\left(-\frac{\omega_1 \hat{V}_1^* + \omega_2 \zeta \hat{V}_2^*}{\hat{V}_{FH}}\right) \quad (5)$$

$$\begin{aligned} \hat{V}_{FH} = & \omega_1 \left(\frac{K_{11}}{\gamma}\right) (K_{21} - T_{g1} + T) \\ & + \omega_2 \left(\frac{K_{12}}{\gamma}\right) (K_{22} - T_{g2} + T) \end{aligned} \quad (6)$$

The self-diffusion coefficients depend on the temperature of the system, and on the mass fraction of solvent and polymer. The mutual diffusion coefficient is function of the solvent self-diffusion coefficient, and is given by the following relation (Equation (7)), with subscripts 1 and 2 referring to solvent and polymer, respectively. ϕ_1 represents the solvent volume fraction, expressed by Equation (8). Equation (7) has been applied in the literature to compute mutual diffusion coefficients for a wide range of drying conditions [4, 32].

$$D^P = D_1(1 - \phi_1)^2(1 - 2\chi\phi_1) \quad (7)$$

$$\phi_1 = \frac{\omega_1 \hat{V}_1^P}{\omega_1 \hat{V}_1^P + \omega_2 \hat{V}_2^P} \quad (8)$$

The partial pressure of the solvent at the surface of the coated layer (p_{li}^G) is equal to the product between the vapor pressure of pure solvent at the actual temperature ($p_{1,v}$) and the activity of the solvent (a_1) [32].

$$p_{li}^G = p_{1,v} a_1 \quad (9)$$

The activity of the solvent is determined with Equation (10) (Flory-Huggins theory), where χ corresponds to the Flory-Huggins interaction parameter.

$$a_1 = \phi_1 \exp[\phi_2 + \chi(\phi_2)^2] \quad (10)$$

The vapor pressure of the pure solvent can be obtained using the Antoine equation [33] – see Equation (11) –, where T is the temperature on the Kelvin scale, and A , B and C are parameters determined for each substance in order to provide an adequate fit of $p_{1,v}$ to the data represented in a phase diagram.

$$\log p_{1,v} = A - \frac{B}{T + C} \quad (11)$$

2.1.2. Energy balance

The coil coating is exposed mainly to radiation and to convective heating from the surrounding air. The temperature of the coating can be assumed to be constant

along the thickness if the resistance of the external heat transport, convection resistance, is significantly higher than the resistance of the internal heat transport, conduction resistance ($Bi \ll 1$). For the case of higher Biot numbers, the constant temperature approximation is no longer valid, the temperature gradients along the coating thickness are no longer negligible and a 1D thermal model is considered, as expressed by Equation (12).

$$\rho^P \hat{C}_p^P \frac{\partial T}{\partial t} = \frac{\partial}{\partial x} \left(k_p \frac{\partial T}{\partial x} \right) + \dot{q}_{tot} \quad (12)$$

In this equation, ρ^P , \hat{C}_p^P , and k_p are the density, the specific heat, and the thermal conductivity of the polymer film, respectively. The source term of the energy equation, \dot{q}_{tot} , takes into account the radiant energy absorbed by the coating – see Equation (13). The radiation intensity through the polymer film is expressed by the Lambert-Beer law.

$$\dot{q}_{tot} = I_0(1 - \rho_{top} - \varepsilon_{top})\alpha \exp(-\alpha d) \quad (13)$$

In Equation (13), I_0 is the intensity of the incident radiation, α is the absorption coefficient, and d corresponds to the traveled distance by radiation. ε_{top} and ρ_{top} are the top surface emissivity and reflectivity, respectively. Considering the axis x with the origin in the substrate-coating interface (see Figure 2), the distance d is equal to the difference between the coating thickness and the x coordinate ($d = X(t) - x$).

Surface energy balances applied at the substrate-coating interface ($x=0$) and at the free surface of the coating ($x=X(t)$) lead to Equations (14) and (15), respectively, which correspond to the boundary conditions of the energy balance equation – Equation (12). In these equations, h^S and h^G are the convection heat transfer coefficients of the substrate-side and coating-side, respectively (see Figure 2), T^S and T^G are the bulk temperatures of the lower gas stream and upper gas stream, respectively, k_{sub} and H are the thermal conductivity and thickness of the substrate, respectively, and $\Delta\hat{H}_v$ is the heat of vaporization of the solvent.

$$-k_p \frac{\partial T}{\partial x} = \frac{T^S - T}{\frac{H}{k_{sub}} + \frac{1}{h^S}} + I_0(1 - \rho_{top} - \varepsilon_{top}) \exp[-\alpha X(t)] \quad (14)$$

$$-k_p \frac{\partial T}{\partial x} = h^G(T - T^G) + k_1^G \Delta\hat{H}_v(p_{li}^G - p_{1b}^G) - I_0 \varepsilon_{top} \quad (15)$$

Equation (15) includes the convective heat transfer with the surroundings (first term on the RHS), the effect of evaporative cooling (second term on the

RHS), and the fraction of incident radiation that is absorbed at the surface of the coating (last term on the RHS). A uniform initial temperature distribution ($T(0, x) = T_0$) is considered in the polymer layer.

Since the species continuity equation for the solvent species and the 1D energy equation are to be solved in a region with a time dependent thickness, due to film shrinkage, it is convenient to immobilize the external polymer phase surface by the introduction of the following transformation expressed in Equation (16), valid for $0 \leq \eta \leq 1$. With this coordinate transformation, the polymer-gas phase interface is always located at $\eta = 1$ [4].

$$\eta = \frac{x}{X(t)} \quad (16)$$

2.2. Macro-scale model: oven hydrothermal model

The macro-scale model solves conservation of mass, momentum, and energy for a fluid flow, in order to obtain fields of velocity, pressure, and temperature, respectively. Additionally, radiation and species conservation are modeled, which provides species distribution and radiative heat exchanges.

The (averaged) continuity and momentum conservation equations – Reynolds-averaged Navier-Stokes (RANS) equations – written in Cartesian coordinates and tensor notation are given by Equations (17) and (18), respectively. In these equations, u_i , ρ , S_m , p , and μ are the (time-averaged) velocity along the Cartesian coordinate i , density, mass source, static pressure, and molecular dynamic viscosity, respectively.

The energy equation is given by Equation (19), where E , k , c_p , Pr_t , h_k , and S_h correspond to the (time-averaged) total energy, thermal conductivity, specific heat, turbulent Prandtl number, specific enthalpy of species k , and heat source, respectively.

$$\frac{\partial \rho}{\partial t} + \frac{\partial}{\partial x_i} (\rho u_i) = S_m \quad (17)$$

$$\begin{aligned} \frac{\partial}{\partial t} (\rho u_i) + \frac{\partial}{\partial x_j} (\rho u_i u_j) = & -\frac{\partial p}{\partial x_i} + \frac{\partial}{\partial x_j} \left[\mu \left(\frac{\partial u_i}{\partial x_j} + \frac{\partial u_j}{\partial x_i} \right. \right. \\ & \left. \left. - \frac{2}{3} \delta_{ij} \frac{\partial u_k}{\partial x_k} \right) \right] + \frac{\partial}{\partial x_j} (-\rho \overline{u'_i u'_j}) \end{aligned} \quad (18)$$

$$\begin{aligned} \frac{\partial}{\partial t} (\rho E) + \frac{\partial}{\partial x_i} [u_i (\rho E + p)] \\ = \frac{\partial}{\partial x_j} \left\{ \left(k + \frac{c_p \mu_t}{Pr_t} \right) \frac{\partial T}{\partial x_j} \right. \\ \left. + \sum_k h_k \left[\frac{\partial}{\partial x_j} (\rho D_{k,m} + \frac{\mu_t}{Sc_t}) \frac{\partial Y_k}{\partial x_j} \right] \right\} + S_h \end{aligned} \quad (19)$$

For species conservation equations, species transport equations are solved through the solution of a convection-diffusion equation, which follows the general form given by Equation (20).

$$\frac{\partial}{\partial t} (\rho Y_k) + \frac{\partial}{\partial x_i} (\rho u_i Y_k) = \frac{\partial}{\partial x_j} \left[\left(\rho D_{k,m} + \frac{\mu_t}{Sc_t} \right) \frac{\partial Y_k}{\partial x_j} \right] + S_k \quad (20)$$

In this equation, Y_k , $D_{k,m}$, μ_t , Sc_t , and S_k are the (time-averaged) mass fraction of species k , diffusion coefficient of species k in the mixture, turbulent viscosity, turbulent Schmidt number, and species k mass source, respectively.

The $k - \varepsilon$ turbulence model is applied to provide the required closure for the set of Equations (18) – (20), *i.e.*, to compute the Reynolds stresses ($\rho \overline{u'_i u'_j}$) according to the Boussinesq (eddy-viscosity) hypothesis and to calculate the required turbulent scalar (energy and species) fluxes [34–36]. In particular, the standard $k - \varepsilon$ model is used to model transport equations for the turbulent kinetic energy (k) and its dissipation rate (ε), which are obtained from the solution of the following set of transport equations – see Equations (21) and (22). In these equations, σ_k and σ_ε are the turbulent Prandtl numbers for k and ε , respectively, P_k ($= -\rho \overline{u'_i u'_j} \partial u_i / \partial x_j$) is the production of turbulent kinetic energy due to velocity gradients, and $C_{\varepsilon 1}$ and $C_{\varepsilon 2}$ are tabulated model constants.

$$\frac{\partial}{\partial t} (\rho k) + \frac{\partial}{\partial x_i} (\rho u_i k) = \frac{\partial}{\partial x_j} \left[\left(\mu + \frac{\mu_t}{\sigma_k} \right) \frac{\partial k}{\partial x_j} \right] + P_k - \rho \varepsilon \quad (21)$$

$$\begin{aligned} \frac{\partial}{\partial t} (\rho \varepsilon) + \frac{\partial}{\partial x_i} (\rho u_i \varepsilon) = & \frac{\partial}{\partial x_j} \left[\left(\mu + \frac{\mu_t}{\sigma_\varepsilon} \right) \frac{\partial \varepsilon}{\partial x_j} \right] + C_{\varepsilon 1} P_k \frac{\varepsilon}{k} \\ & - \rho C_{\varepsilon 2} \frac{\varepsilon^2}{k} \end{aligned} \quad (22)$$

Radiation heat transfer is modeled using the discrete ordinates method (DOM) to solve the radiative transfer equation (RTE). This method is based on the discretization of the radiative intensity directional variation in the total solid angle range 4π – for a comprehensive method description see References [37, 38].

2.3. Numerical models

The set of equations that comprise the micro-scale mathematical model are discretized using finite-differences along the thickness, in a uniform mesh. The

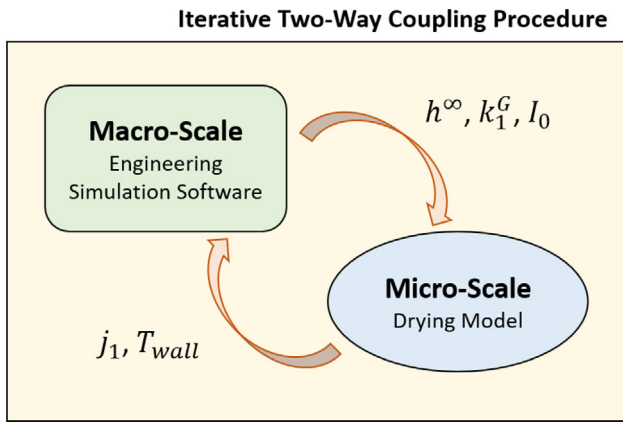


Figure 3. Schematic representation of the iterative two-way coupling procedure adopted in the present work.

nonlinear and differential/algebraic equation solver SUNDIALS numerical model [39] was implemented conveniently to the present work. The macro-scale model was solved numerically using the commercial software ANSYS Fluent 16.2, for steady-state conditions. ANSYS Fluent default turbulence model parameters were considered in this study. Radiatively non-participating medium was considered due to the small optical thickness.

2.4. Coupling methodology

The methodology adopted for the multi-scale modeling is shown in Figure 3 by clarifying the data fluxes, that couple both simulations in an iterative coupling fashion. h^∞ is the convection coefficient of the flow stream (h^G and h^s), j_1 the solvent diffusive mass flux, and T_{wall} the temperature of the metal strip. The multi-scale model developed in the present work considers an iterative two-way coupling procedure between the micro- and macro-scale models, following the steps illustrated in Figure 4. The multi-scale models domains are divided into i zones, in order to obtain more accurate results. In the macro-scale, spatial zones are considered while in the micro-scale a coordinate change, taking into consideration the metal strip velocity, is performed to obtain the corresponding temporal zones.

The procedure begins with the numerical simulation of the macro-scale model considering guessed, and uniform initial values for the top and bottom metal strip temperatures, and for the solvent diffusive mass flux (T_{init} and $j_{1,\text{init}}$). When convergence is achieved, heat transfer coefficients (h^G and h^s), solvent mass transport coefficient (k_1^G), and net radiation heat flux at the metal strip (q''_{rad}), are calculated for each spatial zone and exported to the micro-scale model.

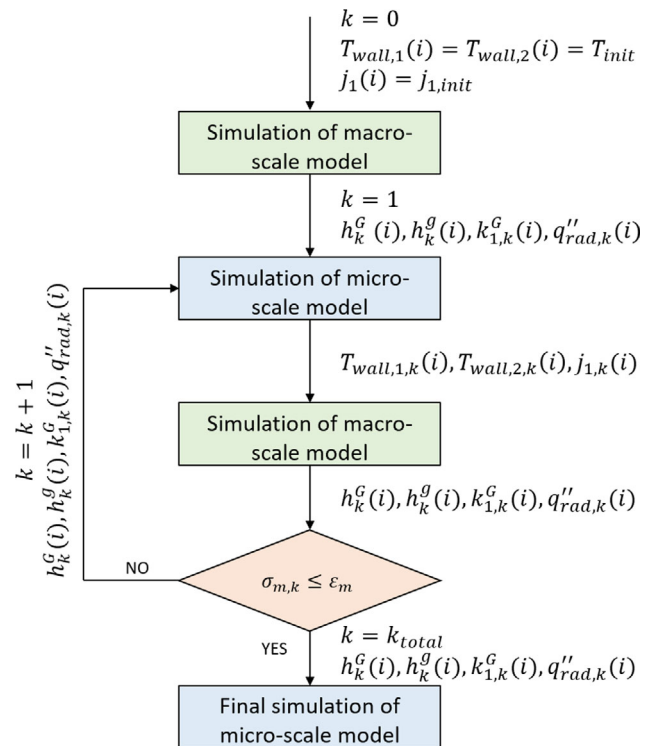


Figure 4. Flow chart of the iterative two-way coupling procedure.

Convective heat transfer and external mass transport coefficients are calculated with custom field functions, based on existing functions in Fluent environment. Equations (23) and (24) describe the two custom field functions used to obtain the coefficients.

$$h^G(i) = \frac{q''_{\text{conv}} G(i)}{T_{\text{wall}}(i) - T_{\text{ref}}} \quad (23)$$

$$k_1^G(i) = \frac{j_1(i)}{p_{1,\text{int}}(i) - p_{1,\infty}} \quad (24)$$

In Equation (23), $q''_{\text{conv}} G$ is the average convection heat flux from the top metal strip surface to the surrounding fluid, and T_{wall} corresponds to the imposed temperature at the metal strip. Convective heat transfer coefficient for the bottom metal strip, h^s , considers, instead, an average convection heat flux from the bottom metal strip surface to the surrounding fluid, $q''_{\text{conv}} g$. In Equation (24), j_1 is the solvent diffusive mass flux at the metal strip top surface, and $p_{1,\text{int}}$ is the average solvent partial pressure at the same surface. The reference temperature and the bulk partial pressure of the solvent, T_{ref} and $p_{1,\infty}$ respectively, were taken to be constant values, since they are auxiliary and internal values of the iterative procedure and do not affect the solution [40]. Nevertheless, the values considered for calculating the coefficients have to be identical to the input values for the micro-scale

model, and have to ensure that there is no signal change and a non-zero result for the denominator of Equations (23) and (24).

The next step initiates the iterative cycle, which starts with the simulation of the micro-scale model considering oven conditions obtained in the previous step. After obtaining the micro-scale model solution, temperature at the interface between the coating and the substrate, temperature at the bottom surface of the substrate, and solvent diffusive mass flux at the coating free surface are evaluated and transferred to the macro-scale model, for the subsequent step. Temperature of the metal strip top surface, $T_{\text{wall},1}$, is directly obtained by solving the 1D energy equation, and corresponds to the temperature of the first mesh point. Temperature of the metal strip bottom surface, $T_{\text{wall},2}$, is achieved through an energy balance at this surface, and is calculated using Equation (25). To obtain solvent diffusive mass flux, j_1 , Equation (24) is applied, with $p_{1,\text{int}}$ determined in the micro-scale model.

$$T_{\text{wall},2} = \frac{\frac{k_{\text{sub}} \times T_{\text{wall},1}}{H} + h^g \times T_{\text{ref}}}{h^g + \frac{k_{\text{sub}}}{H}} \quad (25)$$

A new simulation with the macro-scale is performed, taking into account the values obtained with the micro-scale model. The present iteration ends by evaluating the relative error of the most critical (sensitive) parameter. In this methodology, $\sigma_{m,k}$ is based on the radiative heat flux of each zone, computed in the actual and previous iteration, and is described by:

$$\sigma_{m,k} = \frac{q''_{\text{rad},k} - q''_{\text{rad},k-1}}{q''_{\text{rad},k}} \leq \varepsilon_m = 5\% \quad (26)$$

The iterative two-way coupling procedure terminates when the convergence criterion is respected for every single zone ($\sigma_{m,k} \leq \varepsilon_m$), and the final simulation of the micro-scale model is completed. For each zone the convergence parameter must not exceed a defined threshold value ($\varepsilon_m = 5\%$) to obtain a converged model solution. If convergence is not observed for all zones, the iteration procedure is repeated but with better guesses for the corresponding model parameters.

Since the micro-scale model is continuous in time and from the macro-scale model averaged values for each (discrete) spatial zone are obtained and exported, a smooth step change for each relevant variable was implemented in the micro-scale model to create a sequence of continuous transitions and to avoid abrupt variable discontinuities along the temporal coordinate. The function applied has the form of

Equation (27), where F_1 and F_2 are the constants before and after the step, respectively, and $2\Delta t$ is the time interval set to the step change – equal to 4.0×10^{-3} s in the present work. An increased stability and robustness for the micro-scale numerical model performance is achieved applying this procedure.

$$f(t) = \frac{F_2 - F_1}{2} \sin \left[\frac{\pi}{2\Delta t} (t - t_1) \right] + \frac{F_1 + F_2}{2} \quad (27)$$

3. Results and discussion

In this section the micro-scale model is validated (Section 3.1) and the application of the multi-scale methodology is demonstrated (Section 3.2). Then a parametric study is conducted to analyze the convection and radiation contribution to evaporation (Section 3.3) and the overall performance of coil coating IR radiation process is investigated (Section 3.4).

3.1. Micro-scale model validation

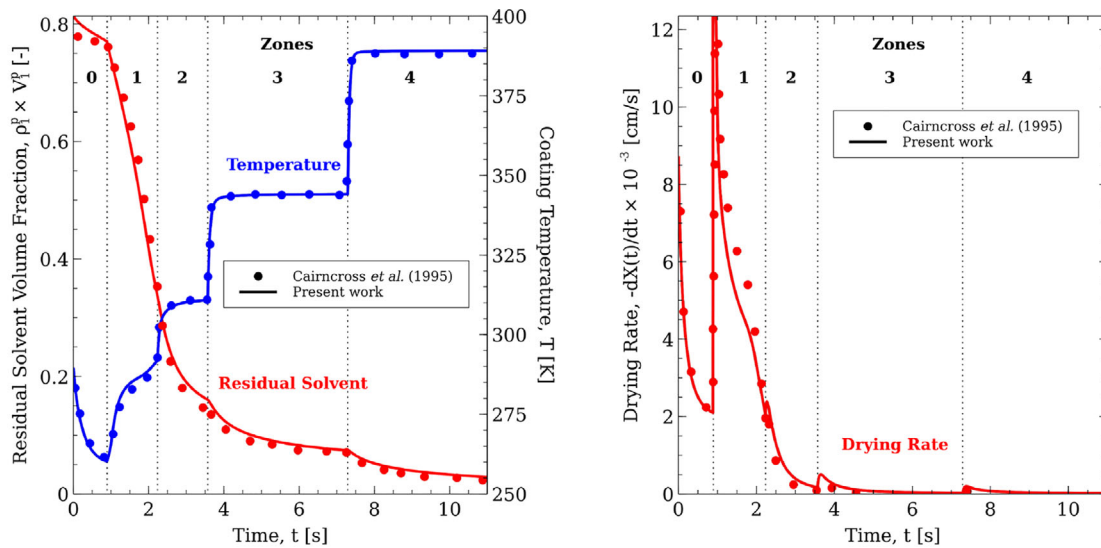
The multi-zone drying of a photoreceptor coating, composed by a methylene chloride/polymer solution, reported by Cairncross *et al.* [27], was selected as a benchmark test case since the interest relies on an industrial dryer with convective and radiant heating. The coating consists in two layers with different infrared radiation absorption characteristics. The thermo-physical properties and parameters of the system, as well as the initial conditions of the problem under consideration are listed in Table 1. The data available in Table 1 was collected from Reference [27]. This data was considered to obtain the numerical results that follow unless otherwise stated.

Two cases are considered, with the first one considering heating of the coating only by convection, and the second takes into account both convection and radiation heating sources. Residual solvent volume fraction, coating temperature, drying rate, and solvent mass density profiles reported in Reference [27] are compared with results from the present work.

The dryer has five different zones, with specific conditions of airflow, and temperature, chosen to achieve an acceptable residual solvent content at the end of the dryer. The residual volume fraction of methylene chloride, V_{res} , is obtained by multiplying the mass density by the partial specific volume of the solvent. Firstly the convective heating is considered and the numerical results obtained are presented in Figure 5(a) for the coating temperature and residual solvent; Figure 5(b) for the drying rate; and Figure

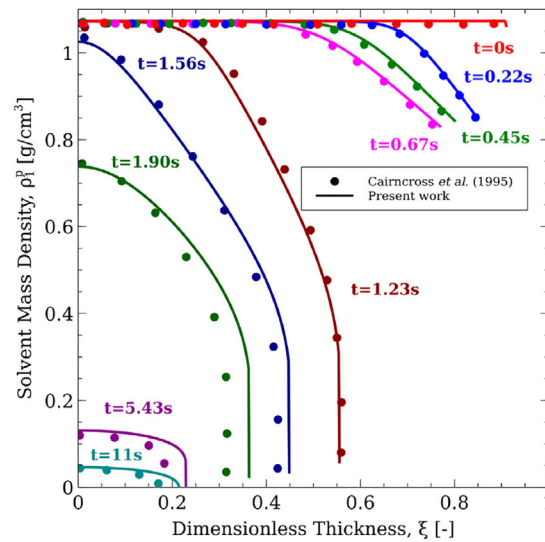
Table 1. Drying model (micro-scale model) properties, parameters, and initial conditions for methylene chloride/polymer solution.

Initial Conditions		Substrate Properties		Diffusion Parameters	
$\rho_{1,0}^p$ [g.cm ⁻³]	1.0732	ρ^s [g.cm ⁻³]	1.38	D_0 [cm ² .s ⁻¹]	2.74×10^{-4}
L [cm]	1.5652×10^{-2}	\hat{C}_p^s [J.g ⁻¹ .K ⁻¹]	1.88	\hat{V}_1^* [cm ³ .g ⁻¹]	0.6247
T_0 [K]	289.15	k_{sub} [W.cm ⁻¹ .K ⁻¹]	1.35×10^{-3}	\hat{V}_2^* [cm ³ .g ⁻¹]	0.733
Coating Properties		H [cm]	3.56×10^{-3}	K_{11}/γ [cm ³ .g ⁻¹ .K ⁻¹]	1.375×10^{-3}
k_p [W.cm ⁻¹ .K ⁻¹]	4.9×10^{-2}	Antoine Eq. Parameters		K_{12}/γ [cm ³ .g ⁻¹ .K ⁻¹]	3.51×10^{-4}
\hat{C}_p^p [J.g ⁻¹ .K ⁻¹]	1.254	A [-]	4.5341	$K_{21} - T_{g1}$ [K]	-19
$\Delta\hat{H}_v$ [J.g ⁻¹]	292.18	B [-]	1325.94	$K_{22} - T_{g2}$ [K]	-290
\hat{V}_1^p [cm ³ .g ⁻¹]	0.7579	C [-]	-20.53	ξ [-]	0.5
\hat{V}_2^p [cm ³ .g ⁻¹]	0.8489	χ [-]	0.28	E/R [K]	0



(a) Coating temperature and residual solvent volume fraction in the system.

(b) Drying rate.



(c) Solvent concentration profiles along the coating thickness.

Figure 5. Comparison between predicted results by the present work and the results reported in Reference [27]. Vertical lines indicate the separation of the dryer zones.

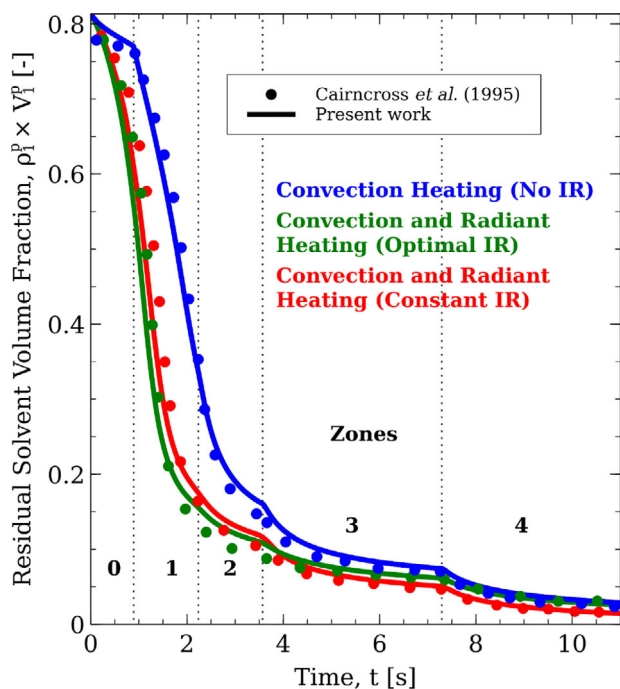


Figure 6. Comparison between predicted results by the present work and the results reported in Reference [27], considering two case studies (convective heating, and convective and radiant heating) for residual solvent volume fraction in the system.

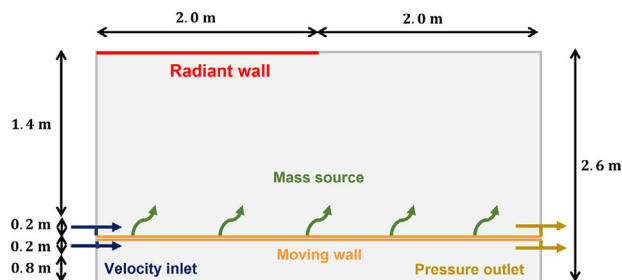


Figure 7. Schematic representation of the 2D oven geometry considered in simulations at the macro-scale level.

5(c) for the solvent mass density profiles. A good agreement between the numerical predictions and the reference data is observed.

Cairncross *et al.* [27] used Lambert-Beer law approximation to describe infrared heating of thin coated layers. Only the fractional thickness $\beta = 0.2$ next to the substrate has an absorption coefficient different from zero ($\alpha = 974.42 \text{ cm}^{-1}$). Equation (28) describes the radiation intensity through the coating.

$$\dot{q}_{\text{tot}} = \begin{cases} I_0 \alpha \exp[-\alpha(X(t) - x)], & 0 \leq x \leq \beta X(t) \\ 0, & \beta X(t) \leq x \leq X(t) \end{cases} \quad (28)$$

Two conditions were analyzed in the reference study: an optimal IR heating, chosen to achieve optimal drying conditions for each dryer zone; and a

constant IR heating source for all the five zones. The numerical results obtained for the second case study, convective and radiant heating, are presented in Figure 6, for the residual solvent volume fraction, along with the predicted results from the current work.

The predictions from the drying model show that heating the coating by IR radiation is favorable mainly in the beginning of the drying. This happens because of the reduction on the effect of the evaporative cooling, and consequently the enhancement of the drying rate. The effect of incident radiation intensity on the solvent content in the coating is shown in Figure 6 for the three cases studied: without infrared radiation; with constant infrared radiation through all dryer zones; and with infrared radiation intensities chosen to optimize drying. In the first three zones, the solvent content is greatly reduced by the additional of radiant heating, while the final residual solvent content is lowered by only 1%. In the last two zones, the high oven temperatures conduct the final residual solvent content in the coating, which make the infrared heating source unnecessary, over convective heating. A good agreement between the numerical predictions and the reference data [27] is observed.

3.2. Multi-scale methodology application

The application of the multi-scale methodology is demonstrated for an idealized 2D (two-dimensional) oven, shown in Figure 7. Boundary conditions are selected in order to appropriately describe the behavior of an industrial curing oven. Since the model in consideration is 2D, the metal strip splits the oven cross section. The metal strip is treated as a hollow region, and is modeled by two surfaces moving from left to right at a velocity v_{wall} . Regarding the source of IR energy, a radiant wall with temperature and emissivity imposed is considered. This wall is located at the first half of the oven, where the metal strip enters. Finally, the iterative procedure calculates the evaporated solvent, injected from a volume mass source boundary condition in a thin layer of cells near the upper wall of the metal strip.

The common mode for drying and curing coil coatings is via convection. To simulate this process, air enters the system at 300 K (T_{in}), with a velocity of 2 m.s^{-1} (v_{in}). The metal strip moves from left to right at 0.363 m.s^{-1} (v_{wall}) and has an emissivity of 0.3 ($\varepsilon_{\text{wall}}$). On the radiant wall, a temperature of 1000 K (T_B) and an emissivity of 0.9 (ε_B) are imposed. Uniform initial conditions are applied, namely the

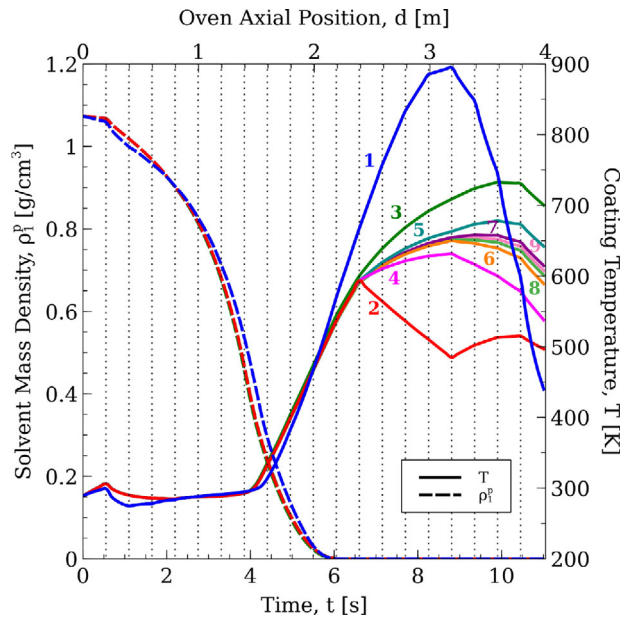


Figure 8. Evolution of solvent mass density and coating temperature along time with the number of iteration of the coupling procedure.

temperature of the metal strip (T_{init}) and the solvent mass source ($S_{1,init}$) – equal to 300 K and $0.1 \text{ kg.m}^{-3}.\text{s}^{-1}$, respectively. (The solvent mass source (S_1) is calculated based on the ratio of the solvent diffusive mass flux and the thickness of the thin layer of cells above the metal strip within which the solvent release is accounted for at the macro-scale level.) The polymer-solvent solution considered is the one used in Reference [27]. The oven was divided longitudinally in 20 equal-sized zones.

Figure 8 shows the evolution of solvent mass density and coating temperature with time (and with oven axial position) for nine iterations of the micro-scale model. After the third iteration the profiles are always between the ones of the last two iterations and the temperature of the coating converged monotonically in nine iterations.

Three distinct zones can be observed in the evolution of the coating temperature with time (or with oven axial position): (i) a first zone from the entrance of the coil in the oven until it traveled 1.5 m, characterized by a constant temperature; (ii) a second zone, where the temperature increases until reaches a maximum value; and (iii) the last zone, with a small decrease on the temperature. In a first stage, the temperature remains approximately constant, since evaporative cooling represents almost the same amount of radiation absorption. At this point, most of the solvent evaporates. The temperature starts increasing, the remaining solvent evaporates, and the temperature reaches a maximum value. The top radiant wall is

Table 2. Injected air and radiant walls conditions for each case study.

Case	Convection			Radiation			
	T_{in} [K]	v_{in} [m.s^{-1}]	T_B [K]	Case	T_B [K]	T_{in} [K]	v_{in} [m.s^{-1}]
C – 1	450	10	–	R – 1	900	300	2.0
C – 2	550	10	–	R – 2	1000	300	2.0
C – 3	550	15	–	R – 3	1100	300	2.0

placed face to face with the coil in the first half of the oven and then in the other half, namely from 3.5 m, only a small amount of net radiative heat flux reaches the coil and the temperature starts decreasing.

3.3. Comparison of convective and radiative conditions on drying behavior

A parametric study is conducted to compare the process efficiency of drying using hot air convection or infrared radiation. The geometry and boundary conditions applied are illustrated in Figure 7. Table 2 lists three different conditions for each main source of energy (convection and radiation) being T_{in} and v_{in} the temperature and the velocity of the air entering the system, and T_B the temperature of the radiant wall. The objective is to find conditions of convective heating and radiative heating that approximately supports similar drying behaviors – *i.e.*, almost the same drying time. For convection cases, no top radiant wall is considered apart from the net radiative power reaching the coil due to the surrounding walls heated by the hot injected air.

Figures 9(a) and 9(b) show the converged multi-scale model evolution of solvent mass density and the dimensionless thickness along time, respectively. Figures 9(a) and 9(b) show that the three selected convective conditions match approximately the corresponding condition of radiation in terms of drying time.

Enthalpy of injected air ($H_{air,in}$), net radiative power reaching the coil (q_{rad}), and power of solvent evaporated ($P_{solv, evap}$) are computed for each case to obtain efficiency values calculated according to Equation (29). The numerator of Equation (29) corresponds to the power consumed for solvent evaporation. Table 3 presents the obtained results of the enthalpy of injected air, the radiative power that reaches the coil, the power of solvent evaporated, and the drying efficiency achieved.

$$\theta = \frac{\int \left[k_1^G (p_{1,i} - p_{1,\infty}) \Delta \hat{H}_v \right] dS}{q_{rad, coil} + H_{air, in}} \quad (29)$$

Table 3 and Figure 9 shows that to evaporate approximately the same amount of solvent, higher

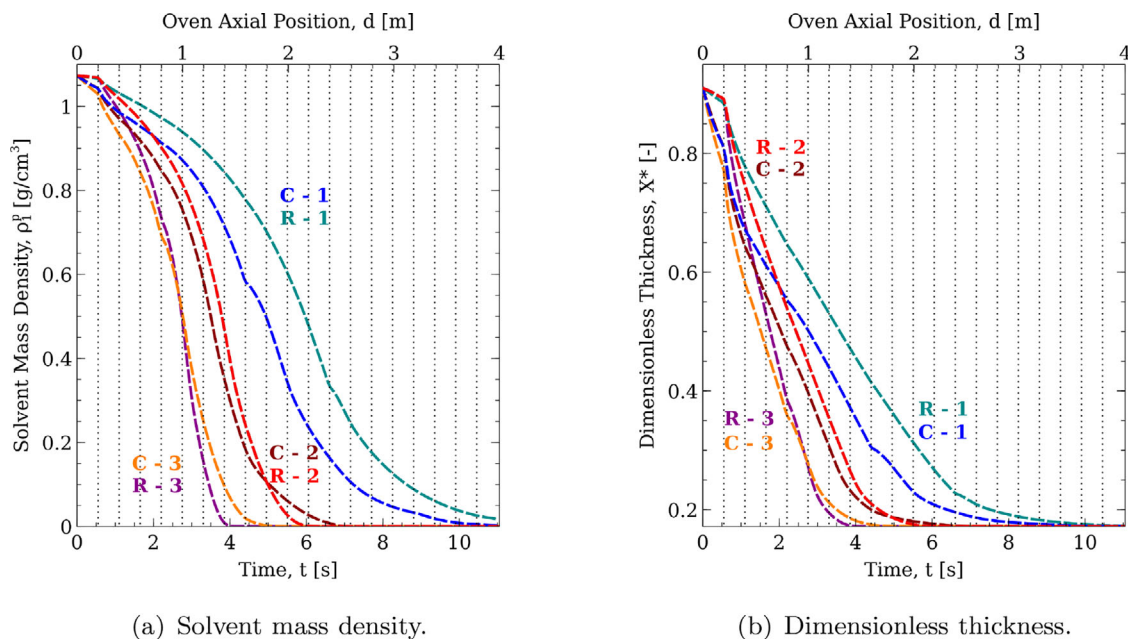


Figure 9. Evolution of converged solutions for a comparison study between convection and radiation.

Table 3. Enthalpy of injected air ($H_{\text{air,in}}$), radiative power reaching the coil (q_{rad}), power of solvent evaporated ($P_{\text{solv, evap}}$), and efficiency (θ), for each case study.

Convection				
Case	$H_{\text{air,in}}$ [kW]	q_{rad} [kW]	$P_{\text{solv, evap}}$ [kW]	θ [%]
C - 1	483.43	1.78	17.69	3.65
C - 2	660.67	2.96	17.51	2.64
C - 3	991.02	3.99	17.58	1.77
Radiation				
Case	$H_{\text{air,in}}$ [kW]	q_{rad} [kW]	$P_{\text{solv, evap}}$ [kW]	θ [%]
R - 1	1.81	20.55	17.63	78.80
R - 2	1.83	28.28	17.74	58.91
R - 3	1.86	32.81	17.77	51.26

efficiencies are achieved with radiation. This comparison example shows how radiative heating stands out over convective heating in terms of energy consumption savings. The industrial implementation of the processes is complex because for the convective mode the heated air in the oven which cools down in the process, mixed with pure air and constantly being preheated by gas-fire burners, may be preheated with the hot evaporated gas. For the radiation mode the evaporated gas is burned in porous radiative burners on the top.

To inspect the requirements to increase convective heating efficiency, and to analyze if there is a possibility to approach radiation efficiencies, several case studies listed in Table 4 were considered. The objective is to study four conditions for each enthalpy of injected air, ranging between 40 and 480 kW. For each power the temperatures of 450, 500, 550, and 600 K correspond to different mass flow rates of air,

and consequently different velocities at the inlet section. Table 4 lists the corresponding inlet velocities for each inlet temperature and enthalpy of air.

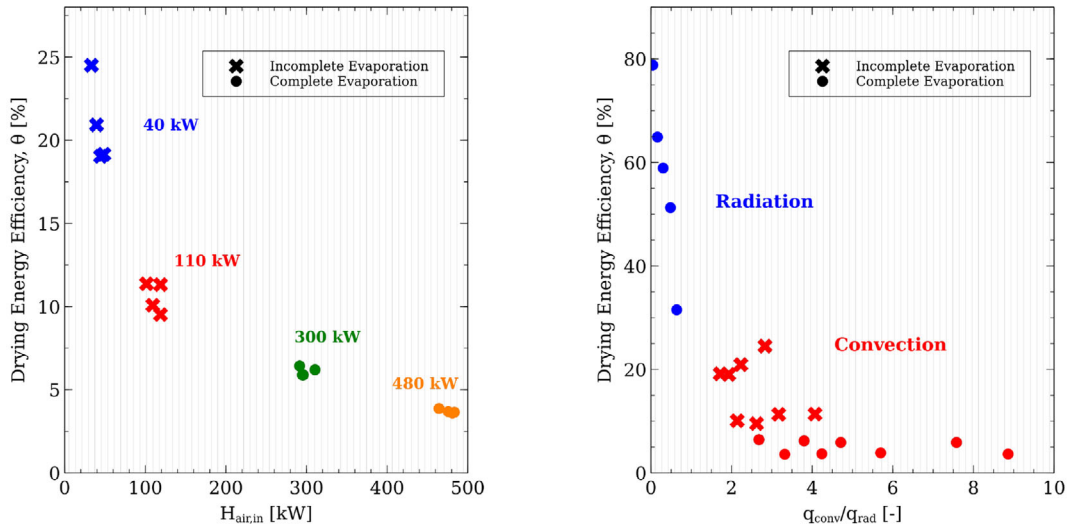
Figure 10(a) shows the calculated efficiency values based on Equation (29), for each case listed in Table 4. The results obtained exhibit an increase on the efficiency when decreasing the enthalpy of air at the inlet section. However, this efficiency improvement means that the solvent does not evaporate completely, *i.e.*, the paint does not dry when passing in the oven under these conditions. Figure 10(b) shows the efficiency as a function of the ratio between convective and radiative heat flux reaching the coil. This ratio is below the unity for radiation dominant cases and above the unity for convection prevailing cases. Two additional radiation case studies, R - 4 ($T_B = 950$ K) and R - 5 ($T_B = 1200$ K), are included to extend the comparison study between convective and radiative heating. The higher efficiencies for the convective heating cases represent a damp product at the end of the oven, since the solvent does not evaporate completely.

3.4. Coil coating IR radiative drying – overall performance

The first step of the coupling procedure is the initial simulation of the macro-scale model with prescribed values of metal strip temperature and solvent mass source, for all the zones in the oven. The geometry and boundary conditions applied are presented in Figure 7. The operating conditions for the macro-scale

Table 4. Injected air velocities for each inlet air temperature and enthalpy.

T_{in} [K]	v_{in} [m.s ⁻¹]			
	$H_{air,in} = 40$ kW	$H_{air,in} = 110$ kW	$H_{air,in} = 300$ kW	$H_{air,in} = 480$ kW
450	0.687	2.06	6.10	10.00
500	0.682	2.05	5.10	8.00
550	0.675	1.80	4.70	7.20
600	0.668	1.50	4.00	6.60



(a) As function of enthalpy of the air injected.

(b) As function of the ratio between convective and radiative heat flux.

Figure 10. Calculated efficiency for a comparison study between convection and radiation. Cross symbols denote incomplete evaporation cases.

Table 5. Operating conditions for the macro-scale model.

T_{in} [K]	v_{in} [m.s ⁻¹]	T_B [K]	ε_B [-]	v_{wall} [m.s ⁻¹]
359	0.101	1600	0.9	0.5

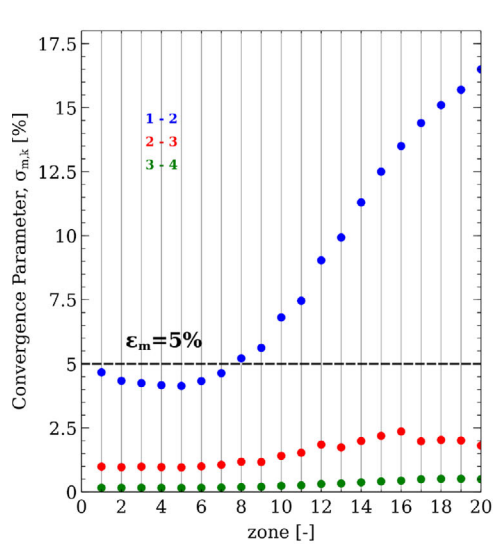
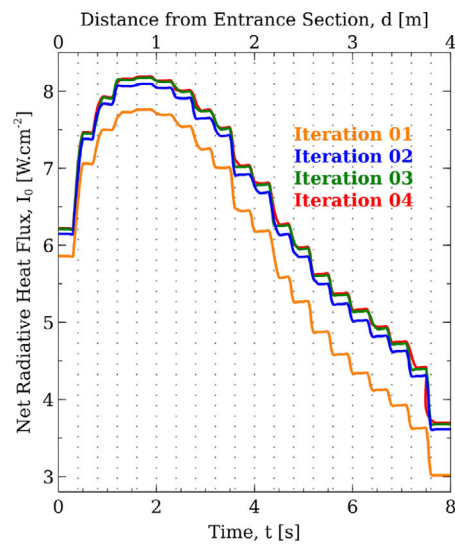
model are listed in Table 5. The metal strip enters at 298.15 K and leaves the oven at 523.15 K. The solvent species considered for this section is the 1,3,5-Trimethylbenzene. The solvent mass source imposed in the first step ($S_{1,init}$) is equal to 1.90 kg.m⁻³.s⁻¹. The injected gas (flue gas) is composed by N₂ (73.2%), H₂O (13.5%), CO₂ (9.7%), and O₂ (3.6%).

Table 6 lists the drying model parameters for 1,3,5-Trimethylbenzene/polymer solution, as well as the initial conditions. The diffusion parameters were obtained based on the method presented by Zielinski and Duda [41]. Antoine equation parameters for calculating vapor pressure of pure solvent and the enthalpy of vaporization of the solvent were collected from Reference [42]. The thermal conductivity of the polymer film (Polyurethane) was obtained from Reference [43]. The substrate considered is hot-dip galvanized (HDG) steel with properties gathered from Reference [44].

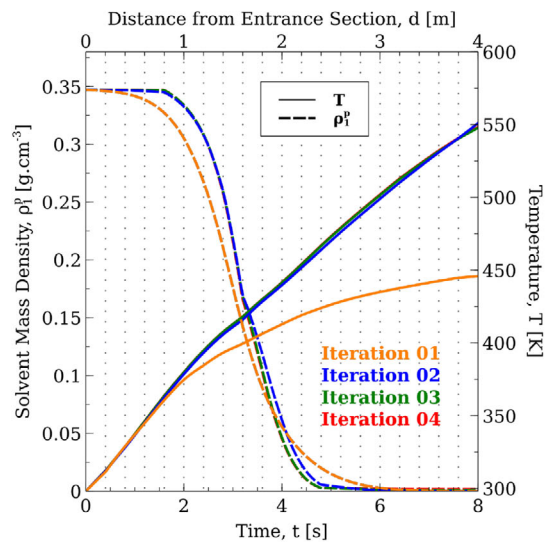
The iterative cycle begins and continues until the convergence criterion is achieved. Due to a good initial guess, only four iterations are required to observe a full convergence. Figure 11(a) shows the evolution of the convergence parameter, $\sigma_{m,k}$ less than 5%, along the number of iteration, for each zone. Figure 11(b) presents the evolution of net radiative heat flux for all the 20 zones considered, with the number of iteration of the coupling procedure. As expected, the maximum incident radiation is near the inlet zone, where the radiant top wall is face to face with the moving coil. Figure 11(c) shows the evolution of solvent mass density and coating temperature along time, for each iteration of the procedure. The metal strip takes 8 seconds to cross the four meters of the oven and all the solvent is evaporated after 5 seconds, as illustrated by the dashed lines. The converged solution of the coating temperature presents a profile approximately linear, similar to the profile imposed at the first iteration. As the coating temperature is constantly increasing, the radiative heat exchange between radiant walls and metal strip starts decreasing, and in turn the net radiative heat flux, illustrated in Figure 11(b), also decreases.

Table 6. Drying model (micro-scale model) properties, parameters, and initial conditions for 1,3,5-Trimethylbenzene/polymer solution.

Initial Conditions		Substrate Properties		Diffusion Parameters	
$\rho_{i,0}^p$ [g.cm ⁻³]	0.3471	ρ^s [g.cm ⁻³]	7.80	D_0 [cm ² .s ⁻¹]	4.52×10^{-3}
L [cm]	3.846×10^{-3}	C_p^s [J.g ⁻¹ .K ⁻¹]	0.470	\dot{V}_1 [cm ³ .g ⁻¹]	0.941
T_0 [K]	298.15	k_{sub} [W.cm ⁻¹ .K ⁻¹]	5.20×10^{-1}	\dot{V}_2 [cm ³ .g ⁻¹]	0.750
Coating Properties		H [cm]	5.00×10^{-2}	Diffusion Parameters	
k_p [W.cm ⁻¹ .K ⁻¹]	2.26×10^{-3}	Antoine Eq. Parameters		K_{11}/γ [cm ³ .g ⁻¹ .K ⁻¹]	1.09×10^{-3}
\hat{C}_p^p [J.g ⁻¹ .K ⁻¹]	6.1511	A [-]	4.1993	$K_{21} - T_{g1}$ [K]	-70.79
$\Delta\hat{H}_v$ [J.g ⁻¹]	384.39	B [-]	1569.62	$K_{22} - T_{g2}$ [K]	-269.5
\dot{V}_1^p [cm ³ .g ⁻¹]	1.4776	C [-]	-63.57	ξ [-]	0.55
\dot{V}_2^p [cm ³ .g ⁻¹]	0.7246	χ [-]	0.44	E/R [K]	0

(a) Convergence parameter, $\sigma_{m,k}$.

(b) Net radiative heat flux along time (and/or distance from the inlet section).



(c) Solvent (1,3,5-Trimethylbenzene) mass density and coating temperature along time (and/or distance from the inlet section).

Figure 11. Evolution of results for coil coating IR radiation overall performance along the number of iteration of the coupling procedure.

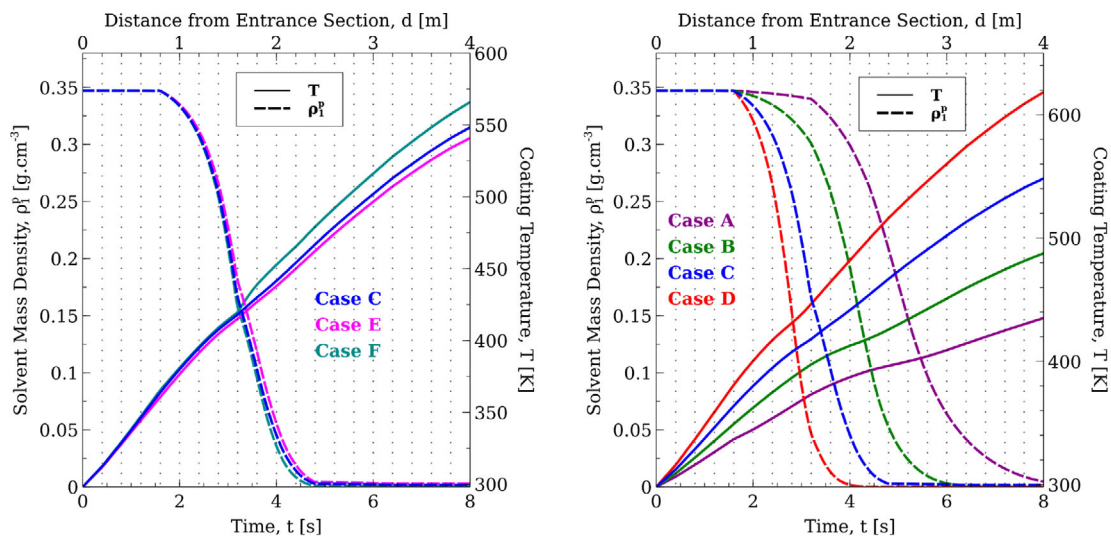
A suitable oven operation requires the complete solvent evaporation from the applied coating at the oven exit section. Under the conditions applied, all the solvent evaporates after going through approximately two thirds of the total length. In order to enhance the process, a decrease on the energy consumption is valuable. Aiming to decrease the time that the dry paint remains in the oven, and

consequently reducing the energy consumption, a parametric study of the temperature on the injected fluid temperature and on the temperature of radiant walls was performed. Table 7 lists the operating conditions implemented for the parametric study. The remaining conditions, namely the metal strip velocity, the velocity of the injected fluid, and the emissivity of radiant walls are kept constant, as described in Table 5.

Table 7. Operating conditions considered for the parametric studies.

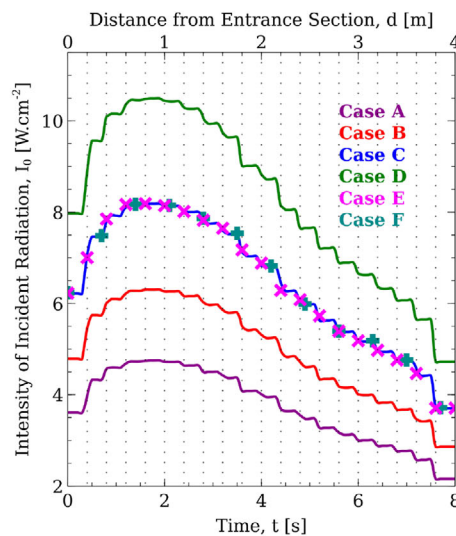
Case	A	B	C	D	E	F
T_B [K]	1400	1500	1600	1700	1600	1600
T_{in} [K]	359	359	359	359	320	450

The iterative two-way coupling procedure is implemented for this parametric study and converged solutions of the micro-scale model are shown in Figures 12(a) and 12(b), varying the injected fluid and the radiant walls temperatures, respectively. Figure 12(c)



(a) Solvent mass density and coating temperature varying the temperature of injected fluid.

(b) Solvent mass density and coating temperature varying the temperature of radiant walls.



(c) Net radiative heat flux for all the cases of the parametric study.

Figure 12. Evolution of results for the parametric study along time (and/or distance from entrance section).

presents the evolution of the net radiative heat flux along time, for the six cases under study. According to Figure 12(a), there is no significant influence of the injected fluid temperature on the drying behavior since radiation plays the most important role on the evaporation process, for the cases under study. Observing the results of Figure 12(b), increasing the temperature of radiant walls speeds up the drying process since the solvent evaporates earlier. For the reference case characterized by the blue color in Figure 12(a)-12(c) it is not beneficial to reduce the drying time, but rather increase it. Therefore, for the same length of the oven and metal strip velocity, a reduction on the temperature of radiant wall increases the drying time and decreases the energy consumption. Concerning the net radiative heat flux, Figure 12(c) shows that changing the injected fluid temperature do not affect the radiative flux reaching the metal strip, seen by overlapping lines. On the other hand, incident radiation increases with higher radiant wall temperature, as expected. The ideal case is then the one considering radiant walls at $T_B = 1400$ K, with injected fluid at $T_{in} = 359$ K, since the paint is dried at the end of the oven with minimal energy supply.

4. Conclusions

A multi-scale model was developed for the IR radiative drying in a coil coating oven. The multi-scale model embraces two different scales: a micro- and a macro-scale. The micro-scale model comprises a drying model which involves simultaneous mass and energy transport. The macro-scale model includes transport phenomena to calculate fluid flow heat transfer in an oven. An iterative coupling procedure between the two models was developed to predict and control the drying behavior of a coated substrate under IR radiant burners. From this investigation the following conclusions can be drawn:

1. A good agreement was obtained between the micro-scale predictions and results from literature of IR heating of thin coated layers;
2. Two drying methods, drying by hot-air flow and by infrared irradiation, were compared. Drying by radiative energy is characterized by minimal energy consumption, low drying time, and consequently, higher efficiencies; and
3. A parametric study was conducted to analyze the influence of coil coating oven operating conditions to provide guidance to achieve good IR radiation design solutions.

Acknowledgements

This research was funded by the European Community's Framework Programme for Research and Innovation Horizon 2020 under grant agreement no. 768692 (ECCO). This work was also supported by FCT, through IDMEC, under LAETA, project UIDB/ 50022/2020.

Disclosure statement

The authors declare no conflict of interest.

References

- [1] Pisano, R.; Fissore, D.; Velardi, S. A.; Barresi, A. A. In-Line Optimization and Control of an Industrial Freeze-Drying Process for Pharmaceuticals. *J. Pharm. Sci.* **2010**, *99*, 4691–4709. <https://www.sciencedirect.com/science/article/pii/S0022354915324072>. DOI: 10.1002/jps.22166.
- [2] Johansson, K.; Johansson, M. A Model Study on Fatty Acid Methyl Esters as Reactive Diluents in Thermally Cured Coil Coating Systems. *Prog. Org. Coat.* **2006**, *55*, 382–387. <https://www.sciencedirect.com/science/article/pii/S0300944006000312>. DOI: 10.1016/j.porgcoat.2006.02.002.
- [3] Perou, A.; Vergnaud, J. Correlation between the State of Cure of a Coil Coating and Its Resistance to Liquids. *Polym. Test.* **1997**, *16*, 19–31. <https://www.sciencedirect.com/science/article/pii/S0142941896000220>. DOI: 10.1016/S0142-9418(96)00022-0.
- [4] Alsoy, S.; Duda, J. Drying of Solvent Coated Polymer Films. *Drying Technol.* **1998**, *16*, 15–44. DOI: 10.1080/07373939808917390.
- [5] Katariya, J.; Arya, R. Drying of Binary Thin Film Polymeric Coatings: An Experimental Study. *Polish Journal. of Chemical. Technology.* **2012**, *14*, 83–87. DOI: 10.2478/v10026-012-0107-0.
- [6] Weinstein, S. J.; Ruschak, K. J. Coating Flows. *Annu. Rev. Fluid Mech.* **2004**, *36*, 29–53. DOI: 10.1146/annurev.uid.36.050802.122049.
- [7] Energy Efficient Coil Coating Process, European Project, **2017**. <https://www.spire2030.eu/ecco>.
- [8] Simmons, G. C.; Lowe, C. A Study on the Adhesion and Flexibility in Radiation-Cured Coil Coatings. *Surface Coatings International Part B Coatings Transactions* **2004**, *87*, 33–40. DOI: 10.1007/BF02699562.
- [9] Yebi, A.; Ayalew, B. Optimal Layering Time Control for Stepped-Concurrent Radiative Curing Process. *Journal of Manufacturing Science and Engineering* **2015**, *137*, 011020. DOI: 10.1115/1.4029023.
- [10] Bombard, I.; Da Silva, B.; Dufour, P.; Laurent, P. Experimental Predictive Control of the Infrared Cure of a Powder Coating: A Non-Linear Distributed Parameter Model Based Approach. *Chem. Eng. Sci.* **2010**, *65*, 962–975. <https://www.sciencedirect.com/science/article/pii/S0009250909006538>. DOI: 10.1016/j.ces.2009.09.050.
- [11] Choi, J. W.; Chun, W. P.; Oh, S. H.; Lee, K. J.; Kim, S. I. Experimental Studies on a Combined near

- Infrared (NIR) Curing System with a Convective Oven. *Prog. Org. Coat.* **2016**, *91*, 39–49. <https://www.sciencedirect.com/science/article/pii/S030094401530268X>. DOI: 10.1016/j.porgcoat.2015.11.004.
- [12] Zhang, M.; Chen, H.; Mujumdar, A. S.; Tang, J.; Miao, S.; Wang, Y. Recent Developments in High-Quality Drying of Vegetables, Fruits, and Aquatic Products. *Crit Rev Food Sci Nutr.* **2017**, *57*, 1239–1255. PMID: 26055086, <https://doi.org/10.1080/10408398.2014.979280>. DOI: 10.1080/10408398.2014.979280.
- [13] EL-Mesery, H. S.; Abomohra, A. E. F.; Kang, C. U.; Cheon, J. K.; Basak, B.; Jeon, B. H. Evaluation of Infrared Radiation Combined with Hot Air Convection for Energy-Efficient Drying of Biomass. *Energies* **2019**, *12*, 2818. <https://www.mdpi.com/1996-1073/12/14/2818>. DOI: 10.3390/en12142818.
- [14] Kowalski, S. J.; Rajewska, K. Convective Drying Enhanced with Microwave and Infrared Radiation. *Drying Technol.* **2009**, *27*, 878–887. DOI: 10.1080/07373930903014837.
- [15] Kinnan, T.; Kondo, Y.; Aoki, M.; Inasawa, S. How Do Drying Methods Affect Quality of Films? Drying of Polymer Solutions under Hot-Air Flow or Infrared Heating with Comparable Evaporation Rates. *Drying Technol.* **2022**, *40*, 653–664. DOI: 10.1080/07373937.2020.1825291.
- [16] Bobba, S.; Zinfullino, N.; Fissore, D. Model-Based Design of Secondary Drying Using in-Line near-Infrared Spectroscopy Data. *Drying Technol.* **2021**, *0*, 1–17. DOI: 10.1080/07373937.2021.2008423.
- [17] Wen, Y. X.; Chen, L. Y.; Li, B. S.; Ruan, Z.; Pan, Q. Effect of Infrared Radiation-Hot Air (IR-HA) Drying on Kinetics and Quality Changes of Star Anise (*Illicium Verum*). *Drying Technol.* **2020**, *39*, 90–103. DOI: 10.1080/07373937.2019.1696816.
- [18] Riadh, M. H.; Ahmad, S. A. B.; Marhaban, M. H.; Soh, A. C. Infrared Heating in Food Drying: An Overview. *Drying Technol.* **2015**, *33*, 322–335. DOI: 10.1080/07373937.2014.951124.
- [19] Sabau, A. S.; Contescu, C. I.; Jellison, G. D.; Howe, J. Y.; Armstrong, B. L.; Daniel, C.; Babinec, S. Evaporation Due to Infrared Heating and Natural Convection. *Heat Mass Transfer* **2020**, *56*, 2585–2593. DOI: 10.1007/s00231-020-02875-0.
- [20] Kumar, S.; Tien, C. L. Analysis of Combined Radiation and Convection in a Particulate-Laden Liquid Film. *Journal of Solar Energy Engineering* **1990**, *112*, 293–300. DOI: 10.1115/1.2929937.
- [21] Lamaison, V.; Scudeller, Y.; Bardon, J. P.; Danes, F.; Peng, S. W.; Dory, J. P. Étude Expérimentale Des Phénomènes de Transfert Lors du Séchage et de la Cuisson de Films de Peinture Sous Rayonnement Infrarouge. *Int. J. Therm. Sci.* **2001**, *40*, 181–194. <https://www.sciencedirect.com/science/article/pii/S1290072900012072>. DOI: 10.1016/S1290-0729(00)01207-2.
- [22] Navarri, P.; Andrieu, J. High-Intensity Infrared Drying Study: Part II. Case of Thin Coated Films. *Chem. Eng. Process* **1993**, *32*, 319–325. <https://www.sciencedirect.com/science/article/pii/0255270193850169>. DOI: 10.1016/0255-2701(93)85016-9.
- [23] Allanic, N.; Salagnac, P.; Glouannec, P. Study of the Drying Behavior of Poly(Vinylalcohol) Aqueous Solution. *Macromol. Symp.* **2005**, *222*, 253–258. <https://onlinelibrary.wiley.com/doi/abs/10.1002/masy.200550433>. DOI: 10.1002/masy.200550433.
- [24] Chen, J. J.; Lin, J. D. Simultaneous Heat and Mass Transfer in Poly627 Mer Solutions Exposed to Intermittent Infrared Radiation Heating. *Numerical Heat Transfer, Part A: Applications* **1998**, *33*, 851–873. DOI: 10.1080/10407789808913970.
- [25] Seyed-Yagoobi, J.; Husain, A. N. Experimental and Theoretical Study of Heating/Drying of Moist Paper Sheet with a Gas-Fired Infrared Emitter. *Journal of Heat Transfer* **2001**, *123*, 711–718. DOI: 10.1115/1.1372324.
- [26] Allanic, N.; Salagnac, P.; Glouannec, P. Convective and Radiant Drying of a Polymer Aqueous. *Heat Mass Transfer* **2007**, *43*, 1087–1095. DOI: 10.1007/s00231-006-0196-5.
- [27] Cairncross, R. A.; Jeyadev, S.; Dunham, R. F.; Evans, K.; Francis, L. F.; Scriven, L. E. Modeling and Design of an Industrial Dryer with Convective and Radiant Heating. *J. Appl. Polym. Sci.* **1995**, *58*, 1279–1290. DOI: 10.1002/app.1995.070580809.
- [28] ul Islam, Z.; Dhib, R.; Dahman, Y. Modeling of Infrared Drying of Polymer Solutions. *Chemical Product and Process Modeling* **2010**, *5*, Article 21. <https://doi.org/10.2202/1934-2659.1488>. DOI: 10.2202/1934-2659.1488.
- [29] Allanic, N.; Le Bideau, P.; Glouannec, P.; Bourmaud, A. Infrared Drying of Water Based Varnish Coated on Elastomer Substrate. *Int. J. Therm. Sci.* **2014**, *79*, 103–110. <https://www.sciencedirect.com/science/article/pii/S1290072914000167>. DOI: 10.1016/j.ijthermalsci.2014.01.013.
- [30] Price, P. E.; Jr.,; Cairncross, R. A. Optimization of Single-Zone Drying of Poly645 Mer Solution Coatings to Avoid Blister Defects. *Drying Technol.* **1999**, *17*, 1303–1311. DOI: 10.1080/07373939908917616.
- [31] Vrentas, J. S.; Duda, J. L. Diffusion of Small Molecules in Amorphous Polymers. *Macro-Molecules* **1976**, *9*, 785–790. DOI: 10.1021/ma60053a019.
- [32] Price, P. E.; Jr., Wang, S.; Romdhane, I. H. Extracting Effective Diffusion Parameters from Drying Experiments. *AIChE J.* **1997**, *43*, 1925–1934. <https://aiche.onlinelibrary.wiley.com/doi/abs/10.1002/aic.690430802>. DOI: 10.1002/aic.690430802.
- [33] Felder, R. M.; Rousseau, R. W. *Elementary Principles of Chemical Processes*; John Wiley & Sons, Inc.: Hoboken, NJ, **2005**.
- [34] Versteeg, H. K.; Malalasekera, W. *An Introduction to Computational Fluid Dynamics: The Finite Volume Method*; Pearson education: Harlow, England, **2007**.
- [35] Ferziger, J. H.; Perić, M.; Street, R. L. *Computational Methods for Fluid Dynamics*; Springer: New York, **2002**; Vol. 3.
- [36] ANSYS Fluent Theory Guide. ANSYS Fluent Theory Guide, **2013**.
- [37] Modest, M. F.; Mazumder, S. *Radiative Heat Transfer* (Fourth Edition); Academic Press: London, **2021**.

- [38] Howell, J. R.; Mengüç, M. P.; Daun, K.; Siegel, R. *Thermal Radiation Heat Transfer* (Seventh Edition); CRC Press: Boca Raton, **2020**.
- [39] Hindmarsh, A. C.; Brown, P. N.; Grant, K. E.; Lee, S. L.; Serban, R.; Shumaker, D. E.; Woodward, C. S. SUNDIALS: Suite of Nonlinear and Differential/Algebraic Equation Solvers. *ACM Trans. Math. Softw.* **2005**, *31*, 363–396. DOI: [10.1145/1089014.1089020](https://doi.org/10.1145/1089014.1089020).
- [40] Navalho, J. E.; Pereira, J. M.; Pereira, J. C. A Methodology for Thermal Analysis of Complex Integrated Systems: Application to a micro-CHP Plant. *Appl. Therm. Eng.* **2017**, *112*, 1510–1522. <https://www.sciencedirect.com/science/article/pii/S1359431116329222>. DOI: [10.1016/j.applthermaleng.2016.10.201](https://doi.org/10.1016/j.applthermaleng.2016.10.201).
- [41] Zielinski, J. M.; Duda, J. L. Predicting Polymer/Solvent Diffusion Coefficients Using Free-Volume Theory. *AIChE J.* **1992**, *38*, 405–415. <https://onlinelibrary.wiley.com/doi/abs/10.1002/aic.690380309>. DOI: [10.1002/aic.690380309](https://doi.org/10.1002/aic.690380309).
- [42] Linstrom, P. J.; Mallard, W. G. The NIST Chemistry WebBook: A Chemical Data Resource on the Internet. *J. Chem. Eng. Data* **2001**, *46*, 1059–1063. DOI: [10.1021/je000236i](https://doi.org/10.1021/je000236i).
- [43] Tsai, P. Y.; Chen, T. E.; Lee, Y. L. Development and Characterization of Anticorrosion and Antifriction Properties for High Performance Polyurethane/Graphene Composite Coatings. *Coatings* **2018**, *8*, 250. <https://www.mdpi.com/2079-6412/8/7/250>. DOI: [10.3390/coatings8070250](https://doi.org/10.3390/coatings8070250).
- [44] Harvey, P. D. *Engineering Properties of Steel*; ASM International: Materials Park, Ohio, **1982**.